

Mechanical properties of porous polymeric nanocomposites reinforced with mesoporous silica nanoparticles and hydroxyapatite: experimental studies and simulations

Masih Nasirshoabi¹ · Nader Mohammadi² · Mehrdad Nasirshoabi²

Received: 23 February 2016 / Accepted: 18 July 2016 / Published online: 23 July 2016
© The Brazilian Society of Mechanical Sciences and Engineering 2016

Abstract Numerical simulations based on finite element analysis (FEA) are increasingly considered essential, important and practical in the course of designing new products these days. Two of the main encountered challenges in using numerical simulation are their ability and precision to predict the mechanical behavior of advanced materials such as polymers or composites. This study demonstrates how mechanical properties and behaviors of porous polymeric nanocomposites can be determined and predicted using tensile loading test data in numerical simulations. The outcome of these simulations could considerably reduce manufacturing cost of these materials in practice. In this study, Polypropylene (PP) has been reinforced with three different types of nanoparticles, mesoporous silica nanoparticles (MSN), hydroxyapatite nanoparticles (HAP), and a mixture of these two. The mechanical tests that were used in this study were tensile test, three-point bending test, and Izod impact test. The final outcome of the tests and their numeric values were numerically simulated using Abaqus FEA software. Knowing that the mechanical behaviors of these materials are determined by

hyperelasticity theory, we used hyperelastic material model to simulate the results. The reason was that this model has different strain-energy density functions. To simulate the tests numerically, the tensile loading test data were used to simulate uniaxial tensile test. The outcome enabled us to draw the related stress–strain curves that were percentage errors of module of elasticity, yield strength, and ultimate strength curves. This was step one of our study. A comparison between these three curves demonstrated that Marlow model could be the best model to predict the actual mechanical behaviors of hyperelastic materials. In the next step, the data generated by tensile loading test were used to carry out numerically simulated bending and Izod impact tests. The outcome demonstrated a close resemblance between simulation results and the tensile loading test results. These results show that numerical simulation can be used to predict mechanical properties of these kinds of materials instead of undertaking costly and time consuming three-point bending and Izod impact tests.

Keywords Abaqus FEA · Polypropylene · Mesoporous silica nanoparticles · Hydroxyapatite nanoparticles · Tensile loading · Three-point bending · Izod

Technical Editor: Dr. Marcelo A. Savi.

✉ Nader Mohammadi
nmohamady@ut.ac.ir

Masih Nasirshoabi
masihnasirshoabi@gmail.com

Mehrdad Nasirshoabi
mehrdadnasirshoabi@gmail.com

¹ Department of Mechanical Engineering, Semnan Branch, Islamic Azad University, 8965151567 Semnan, Iran

² Department of Mechanical Engineering, Parand Branch, Islamic Azad University, 3761396361 Tehran, Iran

1 Introduction

Due to their light weight and powerful capabilities in terms of energy absorption, polymeric foams have gained a large deal of attention in recent years. Being very useful in terms of energy absorption, these materials have been used as energy absorbers in such applications as car bumpers, helmets, drawing chairs, etc. Determination of materials' mechanical properties is a significant step towards designing new products. Numerical simulation is a basic principle

in engineering applications, because it contributes to optimize different components based on the analysis of stress field under various loading conditions, geometries, or with replaced materials. Whenever the simulation results are in good agreement with experimental data, the simulation process will be able to describe mechanical behavior of the material at a good level of accuracy.

In recent years, numerous researches have done on the analysis of mechanical behavior exhibited by similar materials.

Arriga et al. [1] studied the convergence of three-point bending test on specimens of polypropylene. For the sake of simulation, they used a linear elastic model which exhibits plastic behavior beyond the yield point. The results of tests on polyamide specimens indicated that the materials' responses may not be modeled as a linear relation between stress and strain.

In Izod impact test, Tvergaard et al. [2] analyzed the effects of thickness on stress and strain fields for specimens of polycarbonate.

In his research, Viot showed that, in spite of uniaxial compression is the most common mechanical test used, but the results from this test alone are insufficient to characterize the foam response to three-dimensional stress states. Therefore, he proposed a new device for hydrostatic stress tests. Hydrostatic compression tests carried out, on polypropylene foams, both quasi statically and at high strain rates. The data obtained from hydrostatic compression test finally used for modelling purposes [3].

Avalle et al. [4] experimentally evaluated mechanical properties of three polymeric foams, namely expanded polypropylene (EPP), expanded polyurethane (PUR), and polyphenylene oxide/polystyrene (PPO/PS), at ambient temperature under two different loading conditions, namely static loading and impact loading. Using energy-absorption diagrams and efficiency curves, the energy absorption properties of foams were investigated.

The performance of expanded polypropylene (EPP) foams has to be studied as a function of several parameters including the foam density, microstructure, and the strain rate imposed during dynamic loading. Bouix et al. [5] investigated compressive strain–stress behavior of polymeric foams over a wide range of engineering strain rates (from 0.01 to 1500 s⁻¹) to study the effects of foam density and strain rate on the initial collapse stress and the hardening modulus in the post-yield plateau region. They used a flywheel for intermediate rates of strain (about 200 s⁻¹); however, for higher strain rates (about 1500 s⁻¹) used a viscoelastic Split Hopkinson Pressure Bar (SHPB) with nylon bars. A range of foam densities (34–150 kg m⁻³) were considered and microstructural characteristics were investigated using two specific foam types.

Chen et al. [6] investigated, both experimentally and theoretically, nonlinear behavior of bumper foams under cycling loading. To study compressible materials, Chen et al. modified the incompressible viscoelastic model proposed by Rajagopal and Srinivasa [7] and expressed it as a function of the principle stretches. The modified model was first used to describe bumper foams. They also proposed a new compressible viscoelastic model to better predict the nonlinear process underwent by bumper foams (under cyclic loading). The new model was expressed separately as the invariants of stretches and the principle stretches. The compressible viscoelastic model and the compressible viscoelastic model were used to describe bumper foams' response to cyclic loadings of constant amplitude and variable amplitude, respectively. Experimental results illustrates that both the compressible viscoelastic and the viscoelastic models can be seen as suitable models to describe bumper foam response to cyclic loading; the compressible viscoelastic model was proved, however, to provide better results when it came to description of deformation at the end of each cycle.

For large-strain deformation of porous hyperelastic materials, Danielsson et al. [8] proposed a micromechanical structure to develop continuum-level constructive models. They showed that strain-energy density function depends on incompressible hyperelastic matrix material, initial level of porosity, and macroscopic deformation. Taking the first derivative of the strain-energy density function with respect to deformation, they came to an expression for stress–strain behavior of the porous hyperelastic material. To predict the stress–strain behavior of the porous matrix a constructive model expressed as a function of the initial porosity and macroscopic loading conditions.

Demiray et al. [9] determined the macroscopic stress–strain relationships by means of a strain energy based homogenization procedure from the behavior of the cellular structure at the mesoscopic level. Also, they adopted spatially periodic 2-D and 3-D lattices for representing open-cell foams.

Colloca et al. [10] studied the mechanical behavior of hollow glass microballoon–epoxy matrix syntactic foams reinforced with carbon nanofibers (CNFs). They showed that the presence of CNFs leads to increased values of strength and modulus in syntactic foams containing 50 vol.% microballoons compared to unreinforced syntactic foams. Also, they used a homogenization technique based on the so-called differential scheme that accounts for particle size and wall thickness polydispersivity along with entrapped matrix voids to interpret experimental results.

Othman et al. [11] described the performance of polyurethane (PU) foam as an internally-reinforced filler material on pultruded composite square cross-section tubes

made of E-glass/polyester resin. They applied various loads to different angle cross-head platens to assess their energy absorption capacity based on quasi-static load–displacement curves. In addition, the interaction properties of the composite and the foam core sheets during the loadings were discussed. Experimental results indicated that the crashworthy structure of the polyurethane (PU) foam-filled specimen enhanced the specific and quasi-static absorbed energies more than the empty composite tubes.

Composite sandwich panels comprising fibre reinforced polymer (FRP) skins and lightweight material cores are being increasingly used in civil engineering. Garrido et al. [12] presented experimental and analytical investigations about the effects of elevated temperature on the shear response of polyethylene terephthalate (PET) and polyurethane (PUR) foams used in composite sandwich panels. Their results showed that with increasing temperature, the shear responses of PET and PUR foams become more markedly nonlinear. In addition, the shear moduli of these foams suffer considerable reductions, particularly for the PET foam; although at ambient temperature (20 °C) the PET foam is three times stiffer than the PUR foam, at 80 °C their shear moduli become similar, being, respectively, 24 and 66 % of those at ambient temperature.

Gover et al. [13] studied polymeric foam efficacy in portable water filled barriers. They found that extruded polystyrene foam functioned well, with a greater thickness of the foam panel significantly reducing the impacting body velocity as the barrier began to translate.

Dynamic stress–strain response of rigid closed-cell polymeric foams by subjecting high toughness polyurethane foam specimens to direct impact with different projectile velocities and quantifying their deformation response with high speed stereo-photography together with 3D digital image correlation investigated by Koohbor et al. [14]. By obtaining the full-field acceleration and density distributions, the inertia stresses at each point in the specimen are determined through a nonparametric analysis and superimposed on the stress magnitudes measured at specimen ends to obtain the full-field stress distribution.

Heat insulating properties of polymeric foams at ambient temperature using the model of coupled heat transfer by conduction and radiation through computer-reconstructed domains investigated by Ferkl et al. [15]. The developed model was validated using experimental data and compared with other approaches, including state-of-the-art homogeneous phase approach (HPA). The model predicts that the radiative heat flux can account for more than one third of the total heat flux in high porosity expanded polystyrene (EPS) or polyethylene (PE) foams and that the equivalent conductivity of polymeric foam can be significantly reduced by the careful balancing of porosity, cell size, wall thickness and strut content.

The aim of this study is numerical modelling of mechanical properties of specimens of EPP polymeric foam using macroscopic method implemented in Abaqus FEA software. The modelling process is performed on the basis of the results obtained from laboratory tests including stress–strain data from uniaxial tensile tests. The results of the proposed model for the naturally disordered polymeric foams indicate the best match with the mechanical properties of the actual material. Since the mechanical behavior of EPP polymeric foams follow the theory of hyperelasticity, the hyperelastic material model was used to investigate the behavior of these kinds of materials in Abaqus FEA software. Considering the nonlinear nature of hyperelastic materials, it is very difficult and even impossible, in some cases, to numerically model these materials. There are several strain-energy density functions proposed for modelling these materials: Ogden, Polynomial, Marlow, Van der Waals, etc. [16–18].

The specimens were produced via mixing molten technique in an extruder (Aslanian Extruder/EM 80/IRAN) and injection molding process performed on specimens according to the corresponding standards of tensile test, three-point bending test, and Izod impact test. The prepared specimens were then subjected to three different tests including uniaxial tensile test, three-point bending test, and Izod impact test.

2 Uniaxial tensile test

2.1 Nanocomposites preparation

Before preparation of nanocomposites samples, polypropylene granules and their compatibilizer were dried in 80 °C for 48 h in a vacuum furnace. Polypropylene granules and polypropylene compatibilizer (PP-GMA) which used for better dispersing of nanoparticles in polypropylene matrix and linking of matrix/reinforcement interface were blended. These nanoparticles were mixed in an internal mixer. This mixer (HAC/HBI 90) included a pair of roller-rotors with high cutting force. Rotating speed of 120 rpm and chamber temperature of 180 °C were applied, and mixing process was continued for 10 min. The resulting compositions were formed with a milling device and three samples were injected. Holder pressure and injection speed were 115 bar and 45 rpm, respectively. Injection mold temperature in extrusion was among 200–220 °C.

2.2 Morphological properties

Image of Mesoporous silica-hydroxyapatite particles in a polypropylene matrix is shown in Fig. 1. The hollow circular cross-sections represent silica-hydroxyapatite particles. As seen in image, these particles have good and homogeneous

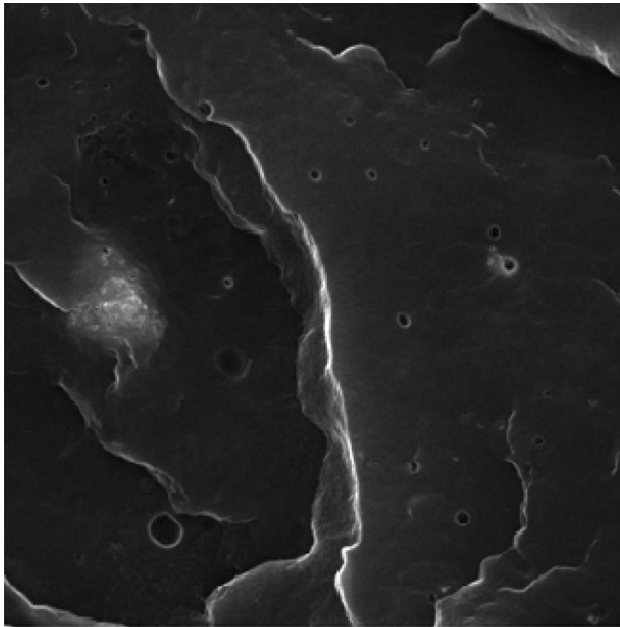


Fig. 1 Image of mesoporous silica-hydroxyapatite particles in a polypropylene matrix

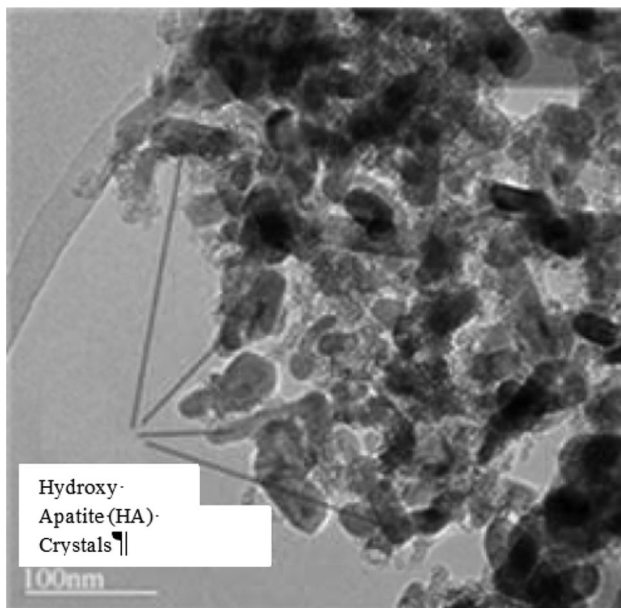


Fig. 2 Hydroxyapatite and mesoporous silica

dispersion. Figure 2 presents image of Mesoporous silica-hydroxyapatite particles in which cylinders are hydroxyapatite and porous particles are mesoporous silica.

The specimens were composed of the following components: polypropylene (PP), polypropylene glycol methacrylate (PP-GMA), mesoporous (MCM-41) and hydroxyapatite (HA) with the following composition percentages:

Table 1 The weight percent of components in each specimen

| Specimens | Components |
|------------|--------------------------------------|
| Specimen 1 | 1 % MCM-41/HA + 2 % PP-GMA + 97 % PP |
| Specimen 2 | 1 % HA + 2 % PP-GMA + 97 % PP |
| Specimen 3 | 1 % MCM-41 + 2 % PP-GMA + 97 % PP |

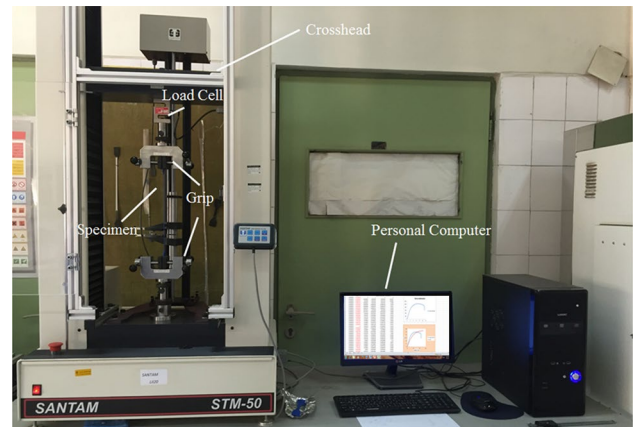


Fig. 3 Santam's universal tensile testing machine (uniaxial tensile test)

According to the three different kinds of material, five specimens for each kind of material were prepared (Table 1).

2.3 Experimental results

Uniaxial tensile test was performed at ambient temperature of 21 °C on three dog-bone specimens on a Santam's universal tensile testing machine (according to ISO 527-2 [19]) (Figs. 3, 4).

Tensile force was gradually applied to the specimens at the constant continuous rate of 5 mm per min, so as they underwent plastic deformation with an ultimate failure. The force and the strain values were recorded by a load cell and a strain gauge extensometer, respectively.

The stress and strain were calculated according to ISO 527-1.

The obtained values of tensile test were converted into nominal stress and nominal strain values using Eqs. (1) and (2), respectively. By the converted values we can draw nominal stress-nominal strain curve.

$$\sigma = \frac{F}{A_0} \quad (1)$$

$$\varepsilon = \frac{L_i - L_0}{L_0} \quad (2)$$

where $L_0 = 50$ mm and $A_0 = 42$ mm².

Fig. 4 A schematic of uniaxial tensile test setup

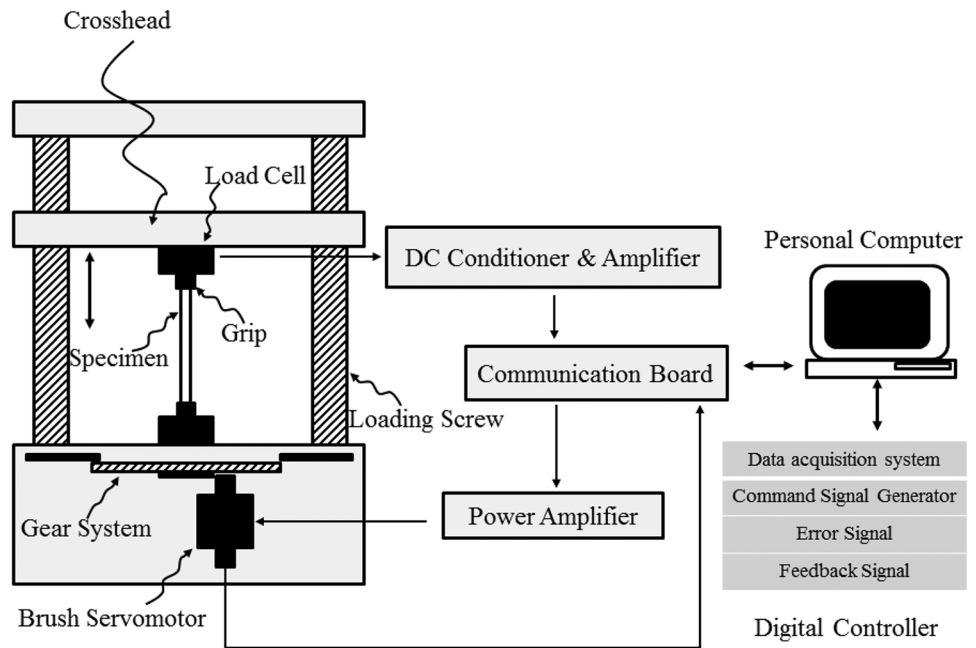
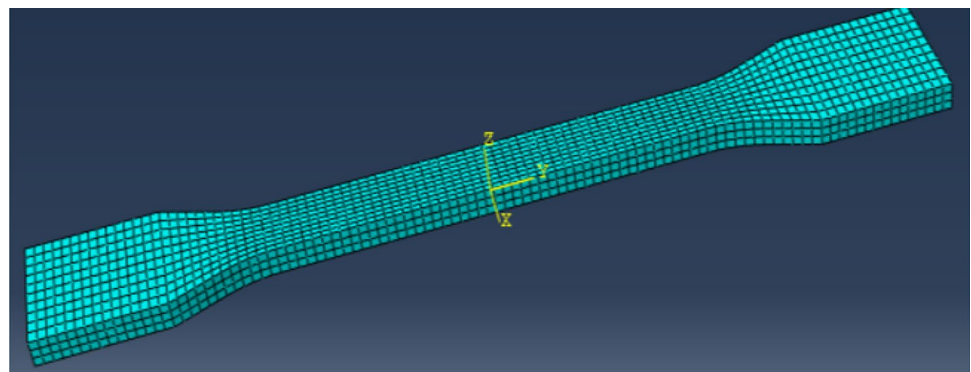


Fig. 5 The gridding of the model



2.4 Simulation of test

Abaqus FEA software provides simulations of tensile tests. According to Fig. 5, the selected elements are three-dimensional hexahedrons with one node at each vertex (each element possess a total of eight nodes) via structure technique. Linear elements geometry is of C3D8R type. This numerical model has 3692 nodes and 2430 elements with the average element size of 1.6 mm.

Hyperelastic model with different strain-energy density functions was used for all simulations. These functions are generally expressed in form of polynomials [20]. We have:

$$U(\epsilon) = \sum_{i+j=1}^N C_{ij}(\bar{I}_1 - 3)^i(\bar{I}_2 - 3)^j + \sum_{i=1}^N \frac{1}{D_i}(J_{el} - 1)^{2i} \quad (3)$$

where $U(\epsilon)$ denotes strain-energy density function, J_{el} is elastic volume ratio, \bar{I}_1 and \bar{I}_2 represent measures of distortion in

the material’s deviant strain, and N , C_{ij} , and D_i are functions of temperature which express material properties.

Three types of strain-energy density functions (i.e., three types of models) are used in the performed simulations. These three models include:

- a) Van der Waals model also known as Kilian model. This model has its name after a similar model used in equations of state describing real gas behavior. The corresponding strain-energy density function can be expressed as follows:

$$U(\epsilon) = \mu \left\{ -(\lambda_m^2 - 3)[\ln(1 - \eta) + \eta] - \frac{2}{3}a \left(\frac{\bar{I} - 3}{2} \right)^{\frac{2}{3}} \right\} + \frac{1}{D} \left(\frac{J_{el}^2 - 1}{2} - \ln J_{el} \right) \quad (4)$$

Table 2 The estimated coefficients of Ogden model by Abaqus FEA

| | <i>i</i> | μ_i | α_i | D_i |
|------------|----------|-------------|-------------|------------|
| Specimen 1 | 1 | -359.039438 | 12.6258853 | 0.00000000 |
| | 2 | 744.883804 | -25.0000000 | 0.00000000 |
| Specimen 2 | 1 | -772.803485 | 9.63194578 | 0.00000000 |
| | 2 | 1294.93340 | -25.0000000 | 0.00000000 |
| Specimen 3 | 1 | -299.313864 | 11.0693142 | 0.00000000 |
| | 2 | 553.811665 | -25.0000000 | 0.00000000 |

where $\tilde{I} = (1 - \beta)\bar{I}_1 + \beta\bar{I}_2$ and $\eta = \sqrt{\frac{\tilde{I}-3}{\lambda_m^2-3}}\mu$ is the initial shear modulus; λ_m is the locking stretch; a is the global interaction parameter; β is an invariant mixture parameter and D governs the compressibility. These parameters can be temperature-dependent. \bar{I}_1 and \bar{I}_2 are the first and second deviatoric strain invariants defined as $\bar{I}_1 = \bar{\lambda}_1^2 + \bar{\lambda}_2^2 + \bar{\lambda}_3^2$ and $\bar{I}_2 = \bar{\lambda}_1^{(-2)} + \bar{\lambda}_2^{(-2)} + \bar{\lambda}_3^{(-2)}$.

- b) Ogden model wherein strain-energy density function is expressed as function of principle stretches; it is expressed as the following equation [18]:

$$U = \sum_{i=1}^N \frac{2\mu_i}{\alpha_i^2} (\lambda_1^{-\alpha_i} + \lambda_2^{-\alpha_i} + \lambda_3^{-\alpha_i} - 3) + \sum_{i=1}^N \frac{1}{D_i} (J_{el} - 1)^{\alpha_i} \tag{5}$$

where N is the material parameter and μ_i, α_i, D_i are temperature dependent parameters. Furthermore, J_{el} denotes the material’s elastic volume ratio and λ_i s are the principle expansions (stretches).

- c) Marlow model strain-energy density function which is solved based on the test data [21]. It is a function of I (the first invariant deviant strain) obtained from the following equation:

$$U = U_{dev}(\bar{I}_1, \bar{I}_2) + U_{vol}(J_{el}) \tag{6}$$

where U_{dev} and U_{vol} are deviatoric and volumetric parts of strain-energy density function; \bar{I}_1 is the first deviatoric strain invariant defined as $\bar{I}_1 = \lambda_1^2 + \lambda_2^2 + \lambda_3^2$.

Table 3 The estimated coefficients of Van der Waals model by Abaqus FEA

| | μ | λ_m | a | β | D |
|------------|------------|-------------|------------|------------|------------|
| Specimen 1 | 232.722160 | 1.95258163 | 5.82000249 | 0.00000000 | 0.00000000 |
| Specimen 2 | 432.392612 | 1.77208549 | 13.3457448 | 0.00000000 | 0.00000000 |
| Specimen 3 | 208.890003 | 1.78612434 | 11.3256716 | 0.00000000 | 0.00000000 |

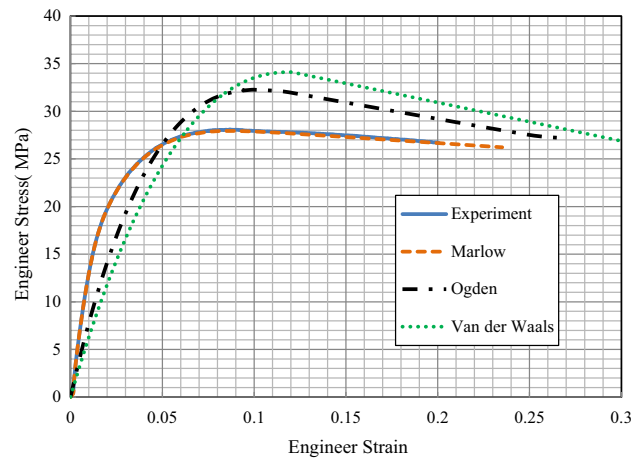


Fig. 6 Stress–strain curves obtained from uniaxial tensile test together with different models: specimen 1

For modelling hyperelastic materials, there are two main approaches to declare material properties in FEA software:

1. By directly declaring the material coefficients.
2. By the use of test data.

In the second approach, the software estimates the coefficients of strain-energy density function according to the data obtained from test; the material coefficients of the hyperelastic models can be calibrated by Abaqus from experimental stress–strain data. In the case of the Marlow model, the test data directly characterize the strain energy potential (there are no material coefficients for this model). This study follows the second approach. Abaqus minimizes the relative error rather than an absolute error measure since this provides a better fit at lower strains. This method is available for all strain energy potentials and any order of $N = 2$ is allowed. The Ogden and Van der Waals potentials are nonlinear in some of their coefficients, thus necessitating the use of a nonlinear least-squares procedure. The estimated coefficients of Ogden and Van der Waals models are provided in Tables 2 and 3. For material calibration, Abaqus requires the Kirchhoff stress versus true strain as input. The Kirchhoff stress accounts for compressibility

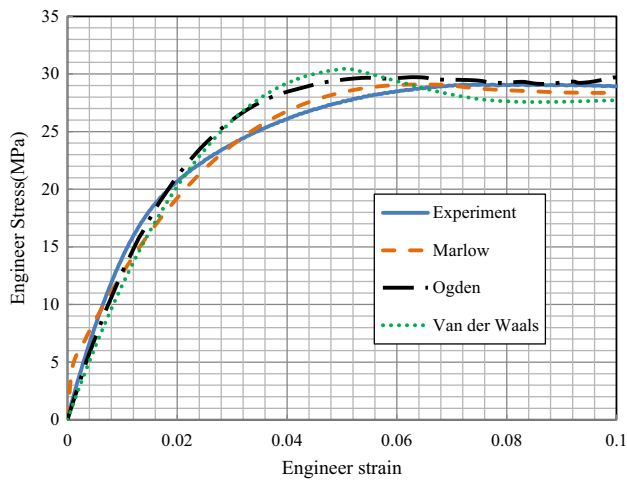


Fig. 7 Stress–strain curves obtained from uniaxial tensile test together with different models: specimen 2

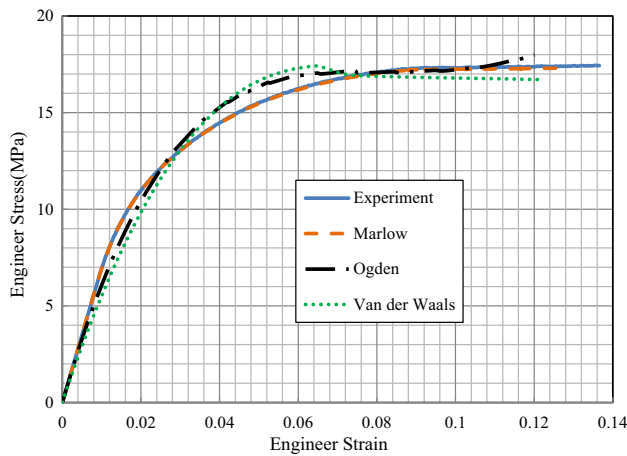


Fig. 8 Stress–strain curves obtained from uniaxial tensile test together with different models: specimen 3

Table 4 The values of stress, strain, and elasticity modulus (for both the model and test) corresponding to the specimen 1

| | Marlow | Van der Waals | Ogden | Experimental |
|------------------|--------|---------------|--------|--------------|
| σ_Y [MPa] | 11.70 | 16.49 | 14.52 | 11.84 |
| ε_Y | 0.008 | 0.015 | 0.012 | 0.007 |
| σ_u [MPa] | 29.08 | 30.40 | 29.71 | 29.05 |
| ε_u | 0.062 | 0.051 | 0.062 | 0.077 |
| E [MPa] | 1462.5 | 1099.3 | 1210.2 | 1691.4 |

through the Jacobian (determinant of the deformation gradient). For incompressible materials, the Kirchhoff stress is equal to the true stress. However, for compressible materials (such as foams), they will differ. These simulations are based on incompressibility assumption.

Table 5 The values of stress, strain, and elasticity modulus (for both the model and test) corresponding to the specimen 2

| | Marlow | Ogden | Van der Waals | Experimental |
|------------------|--------|--------|---------------|--------------|
| σ_Y [MPa] | 9.84 | 14.52 | 16.49 | 11.84 |
| ε_Y | 0.006 | 0.012 | 0.015 | 0.007 |
| σ_u [MPa] | 29.08 | 29.71 | 30.40 | 29.05 |
| ε_u | 0.062 | 0.062 | 0.051 | 0.077 |
| E [MPa] | 1640.1 | 1210.2 | 1099.3 | 1691.4 |

Once finished with simulating the tensile test in Abaqus software, the corresponding data to actual stress and actual strain was extracted for all three models (Van der Waals, Ogden, and Marlow models). To compare the stress–strain curves obtained from these three models with those of tests, we should convert simulation results into engineering stress and engineering strain via the following equations:

$$\varepsilon_{\text{true}} = \ln(1 + \varepsilon_e) \rightarrow \varepsilon_e = e^{\varepsilon_{\text{true}}} - 1 \tag{7}$$

and,

$$\sigma_{\text{true}} = \sigma_e(1 + \varepsilon_e) \rightarrow \sigma_e = \frac{\sigma_{\text{true}}}{1 + \varepsilon_e} \tag{8}$$

where σ_{true} , $\varepsilon_{\text{true}}$, σ_e and ε_e denote actual stress, actual strain, engineering stress and engineering strain, respectively.

Figures 6, 7, 8 demonstrate the stress–strain curves obtained from uniaxial tensile test together with different models for each of the three specimens.

According to the Figs. 6, 7 and 8, in specimens 1 and 3, Marlow model has the highest agreement with the test data. In the following elasticity modulus percentage error, yield strength, and ultimate strength corresponding are compared to the three models for the specimen 1.

2.5 Elasticity modulus, yield strength, and ultimate strength percentage errors

Elasticity modulus (E) (according to ISO 527-1), yield strength (σ_Y), and ultimate strength (σ_u) percentage errors can be obtained via the following equations:

$$E_{\text{experimental}} = \frac{(\sigma_Y)_{\text{experimental}}}{(\varepsilon_Y)_{\text{experimental}}}, E_x = \frac{(\sigma_Y)_x}{(\varepsilon_Y)_x}$$

$$E_{\text{percent of error}} = \frac{E_x - E_{\text{experimental}}}{E_{\text{experimental}}} \times 100 \tag{9}$$

$$\sigma_Y \text{ percent of error} = \frac{(\sigma_Y)_x - (\sigma_Y)_{\text{experimental}}}{(\sigma_Y)_{\text{experimental}}} \times 100$$

$$\sigma_u \text{ percent of error} = \frac{(\sigma_u)_x - (\sigma_u)_{\text{experimental}}}{(\sigma_u)_{\text{experimental}}} \times 100$$

Table 6 The values of stress, strain, and elasticity modulus (for both the model and test) corresponding to the specimen 3

| | Marlow | Ogden | Van der Waals | Experimental |
|------------------|--------|--------|---------------|--------------|
| σ_Y [MPa] | 7.23 | 10.07 | 9.71 | 7.78 |
| ε_Y | 0.0105 | 0.019 | 0.019 | 0.0115 |
| σ_u [MPa] | 16.51 | 17.17 | 17.39 | 16.23 |
| ε_u | 0.063 | 0.074 | 0.065 | 0.061 |
| E [MPa] | 688.57 | 512.67 | 494.14 | 676.52 |

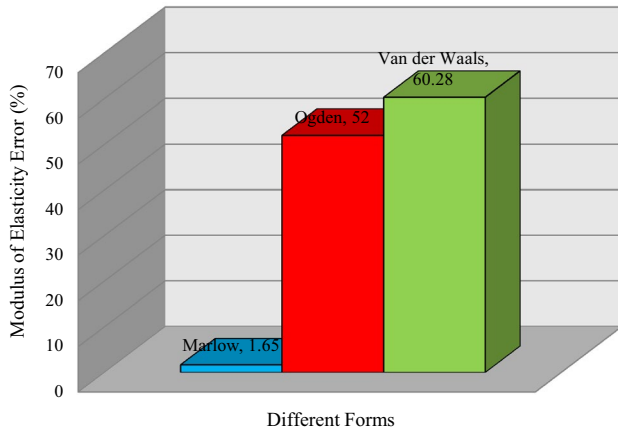


Fig. 9 Bar chart of elasticity modulus percentage error, specimen 1

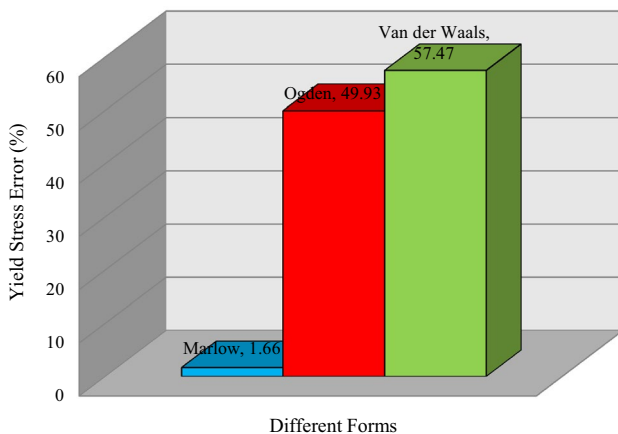


Fig. 10 Bar chart of yield strength percentage error, specimen 1

where ε_Y and ε_u are yield strain and ultimate strain, respectively. Tables 4, 5, 6 report the values of stress, strain, and elasticity modulus (for both the model and test) corresponding to the specimens 1, 2, and 3.

It is observed that in all simulations the Marlow model has acceptable adaptation with experimental parameters. Also, it is obvious that adding nanoparticles (MCM-41 and

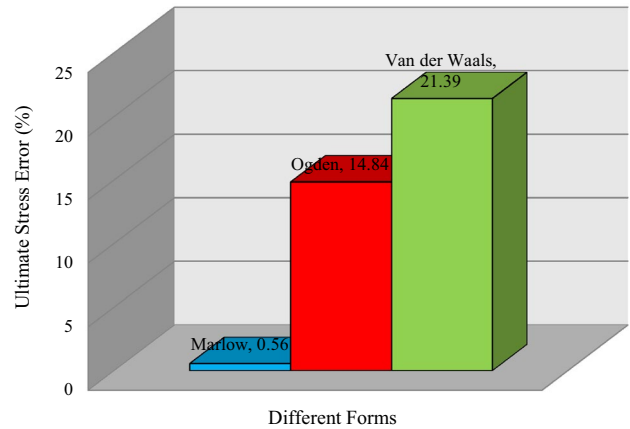


Fig. 11 Bar chart of ultimate strength percentage error, specimen 1



Fig. 12 Three-point bending test machine

PP-GMA) to polypropylene improve the mechanical properties of specimens such as yield stress and ultimate stress.

Figures 9, 10, 11 demonstrate the bar charts of elasticity modulus (E), yield strength (σ_Y) [MPa], and ultimate strength (σ_u) [MPa] percentage errors corresponding to the specimen 1.

The Figs. 9, 10, 11 illustrate that the Marlow model has the lowest error among the other models in numerical simulation.

3 Three-point bending test

3.1 Experimental results

According to ASTM D790-03 [22], three-point bending test was conducted on the specimens of $150 \times 10 \times 4.2$ mm dimensions. Figures 12 and 13

Fig. 13 Three point bending test setup

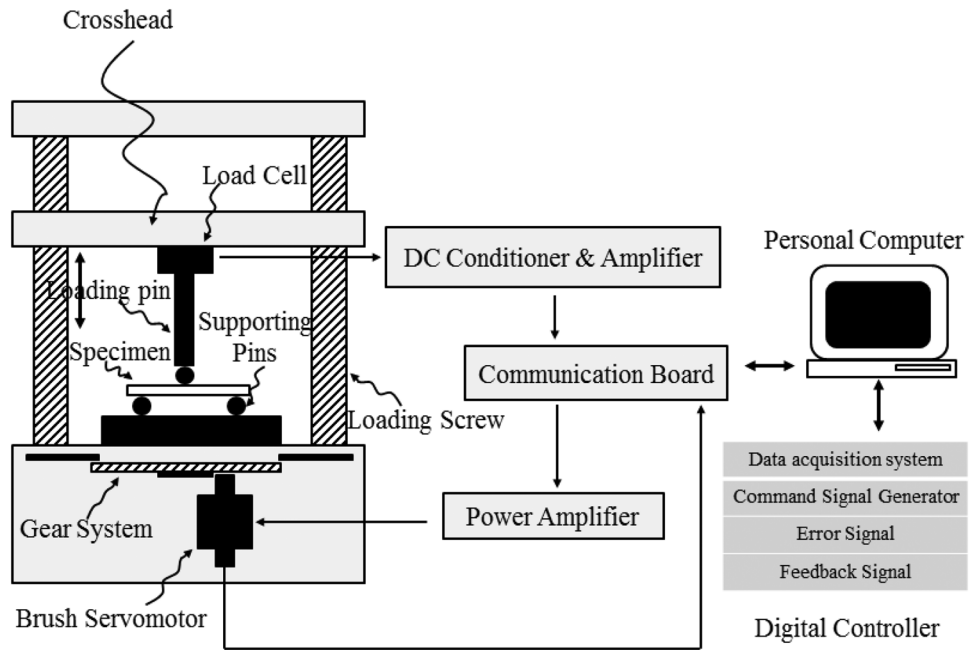


Fig. 14 Linear meshing

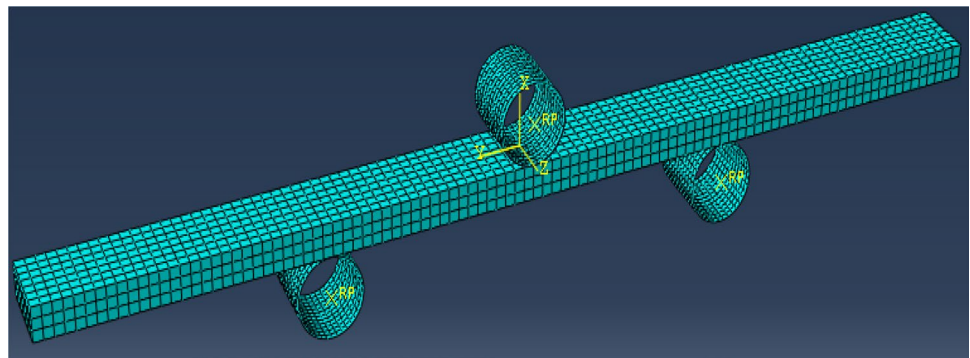
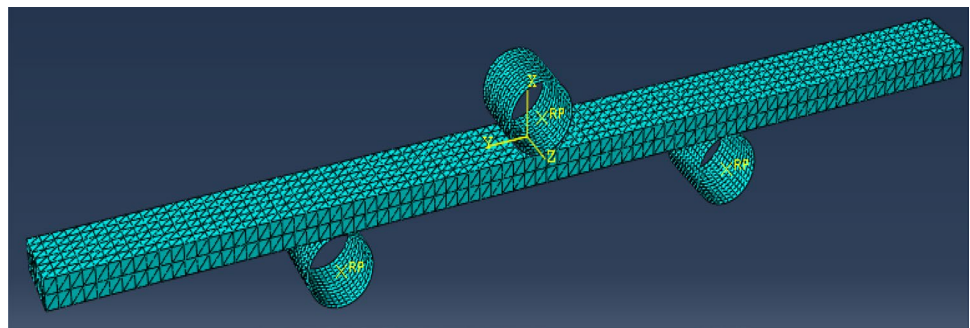


Fig. 15 Second order meshing



show the three-point bending test machine along with the test setup. Specimens were placed on supporting pins of 64 mm distance from one another. The loading pin’s downward movement speed was set to 1.7 mm min^{-1} . The loading rate in bending tests is normally fluctuating within $0.1\text{--}10 \text{ mm min}^{-1}$. Force-related data was recorded by a load cell unit.

3.2 Simulation of three-point bending test

Abaqus FEA software was utilized to simulate bending test. In the part section, R3D4 rigid shell element was used to model constraints corresponding to the loading pin and supporting pins. In the property section, the Marlow form was selected for the hyperelastic material. Furthermore, in

Fig. 16 Model deformation in the course of bending simulation

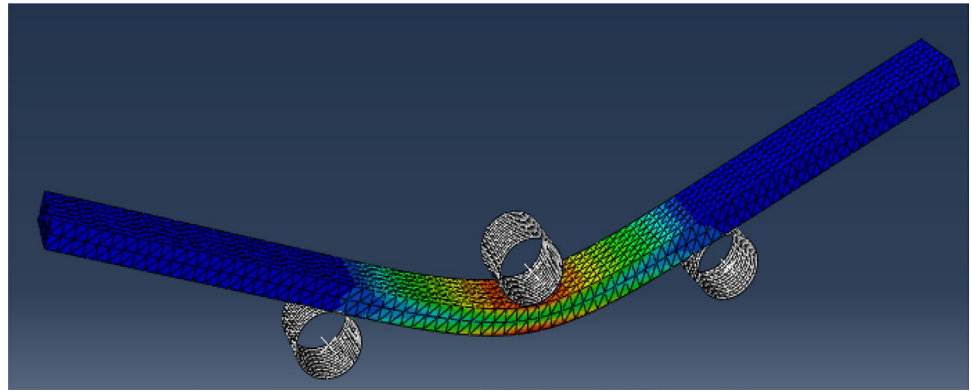
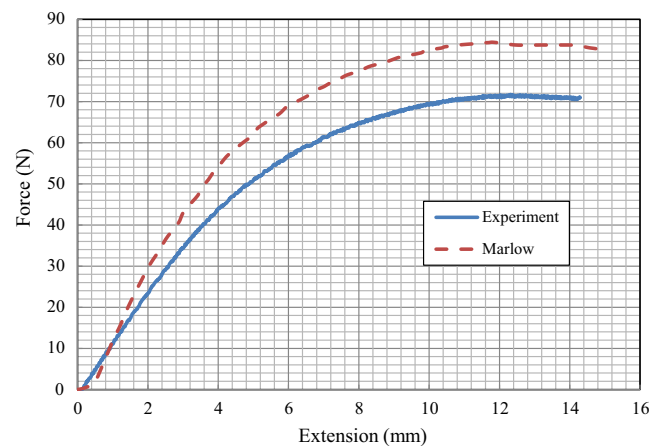


Fig. 17 Force–displacement curves obtained from test data and simulation results, specimen 1



the step section, the dynamic implicit solution was selected to solve the problem. In the interaction phase, surface-to-surface command across different surfaces was used to define the contact surface with a friction coefficient of 0.25. In the load section, the two underneath shells were constrained on all sides with the upper shell moving downward at $0.02833 \text{ mm s}^{-1}$.

Two different meshing approaches are followed here (Figs. 14, 15):

- a) C3D4H (linear)
- b) C3D10H (quadratic)

The rigid components had 1560 nodes and 1443 elements with the average element size of 0.8 mm. The models had 18,666 nodes and 11,304 elements with the average element size of 1.8 mm.

In the linear meshing approach, a considerable amount of dispersion was observed within the results which represent unacceptable convergence (the convergence criterion is defined as the closeness of the resultant curve from simulation to the curve obtained from test data; with linear meshing, a while after starting to run the simulation in the software, we dealt with an error message) across the results.

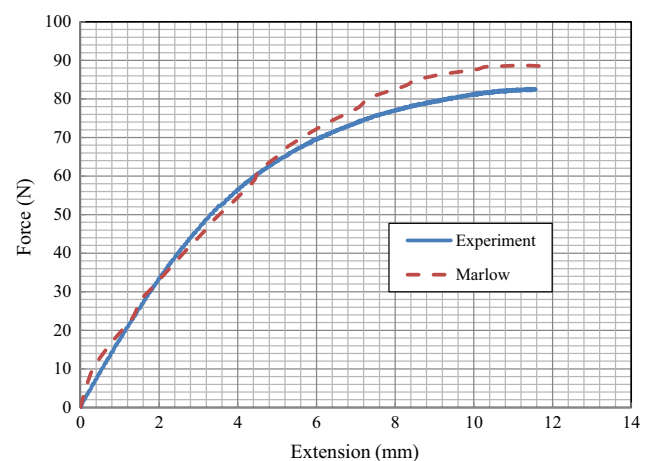


Fig. 18 Force–displacement curves obtained from test data and simulation results, specimen 2

(Because with a little data available due to errors encountered during the simulation process, we may not achieve an acceptable curve). Therefore, first order elements seem not to be adequate for bending simulations. Second order meshing, however, gave acceptable convergence. Although the second order meshing, took much longer time, compared

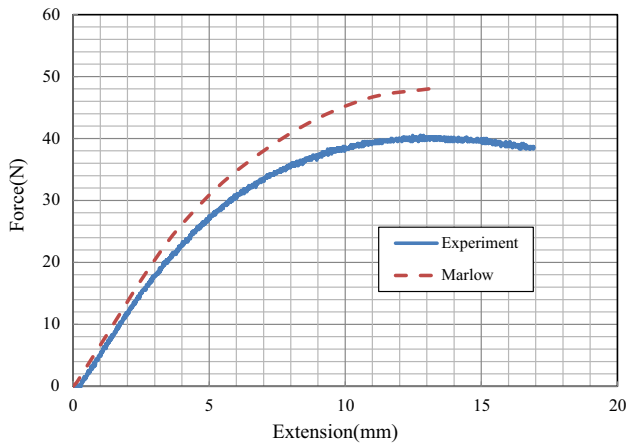


Fig. 19 Force–displacement curves obtained from test data and simulation results, specimen 3

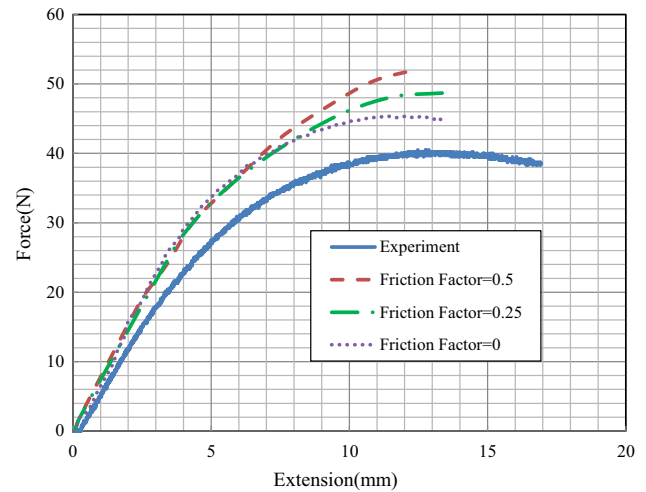


Fig. 21 Contribution of friction coefficient into the force–displacement curve, specimen 3

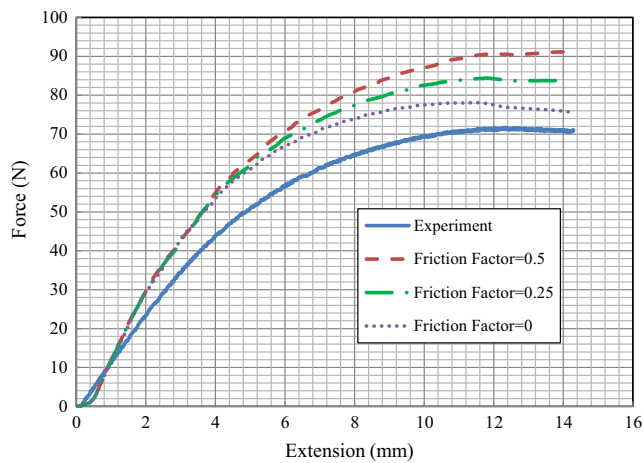


Fig. 20 Contribution of friction coefficient into the force–displacement curve, specimen 1

to that of the linear meshing, but it returned better results. Figure 16 shows the specimens deformation in three-point bending test simulation.

Figures 17, 18, 19 present the force–displacement curves corresponding to the three specimens and have them compared with the experimental values.

In Figs. 20 and 21 the results of force–displacement simulation curves for the specimens 1 and 3 at three different friction coefficients ($\mu = 0, 0.25, \text{ and } 0.5$) are compared to those obtained from test. The figures show that the lower the friction coefficient, the closer will be the simulation-derived force–displacement curve to that obtained from test data. This is because the lower the friction coefficient, the lower force is required by the upper shell to impose deformations into the specimen. In the case of bending simulations, the imposed friction coefficient influences the results



Fig. 22 Izod impact test machine

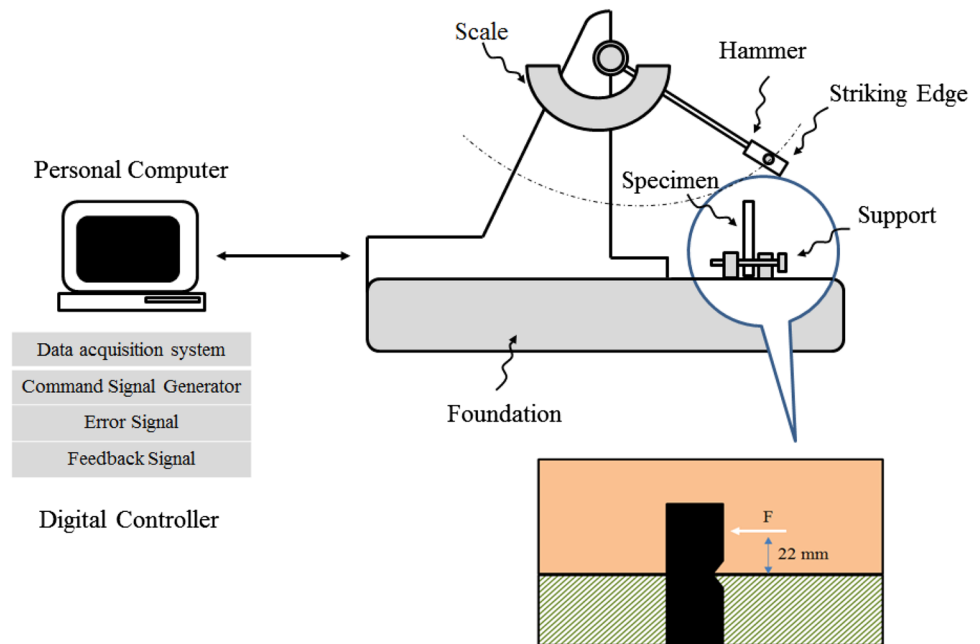
only after the specimens start to slip between the supports. The simulations overestimate the reaction forces regardless of the friction coefficient. It is worth mentioning that, in the course of bending simulation, the center of the upper shell was taken as the point from which the force-related values were measured; it is commonly referred to as the reference point.

4 Izod impact test

4.1 Experimental results

Izod impact test is often used to measure the strength of a material against impact loading. In this test, notched specimens of specified dimensions were prepared and then the

Fig. 23 A schematic view of Izod impact test setup



Izod impact test was done on them using the Izod impact test machine according to ASTM D246. Figures 22 and 23 represent the impact test machine and test setup, respectively. Notched specimens were vertically placed between the supports and then the pendulum was released from an initial position at 150° , so that it hit the free end of the specimen at 3.46 m s^{-1} . The screen displayed the absorbed energy immediately after the specimen was fractured. The test was undertaken at 21°C .

To achieve more accurate results, the Izod impact test was repeated 3–5 times for each specimen. The average of the achieved results was chosen as the absorbed energy for each specimen (Table 7). As we see in Table 7 the absorbed energy results show high dispersion. One of the reasons is the quality of specimens during the mixing and injection processes. Because after the end of Izod impact test for each specimen, it was shown that there are hollows in some of them which could impress the results of the test. For this reason five repetitions were done for each specimen.

4.2 Simulation of Izod impact test

The specimens were modeled in the software according to ASTM D256. In the part section, R3D4 rigid shell element was used to model the pendulum. To apply boundary conditions onto the model, Encastre command was used to fully constraint the model up to the notch. In the load section, the two underneath shells were constrained on all sides with the upper shell moving downward at $0.02833 \text{ mm s}^{-1}$. In mesh part, a three-dimensional hexahedron element with one node at each vertex was chosen with linear geometry (Fig. 24). The rigid shell element had 255 nodes and 238

Table 7 The results of Izod impact test

| Specimen | Test repetition | Absorbed energy (J) | Average of absorbed energy (mJ) |
|------------|-----------------|---------------------|---------------------------------|
| Specimen 1 | 1 | 0.085 | 85 |
| | 2 | 0.079 | |
| | 3 | 0.089 | |
| | 4 | 0.085 | |
| | 5 | 0.087 | |
| Specimen 2 | 1 | 0.075 | 111.6 |
| | 2 | 0.107 | |
| | 3 | 0.073 | |
| | 4 | 0.158 | |
| | 5 | 0.145 | |
| Specimen 3 | 1 | 0.069 | 132.6 |
| | 2 | 0.129 | |
| | 3 | 0.144 | |
| | 4 | 0.157 | |
| | 5 | 0.164 | |

elements with the average element size of 0.4 mm. The model had 56,265 nodes and 49,200 elements with the average element size of 0.4 mm.

In Fig. 25 the impact energy corresponding to each specimen at different instances versus time was plotted. In contrary, to the tests where specimens actually break under the impact, we cannot observe such a breakage in the software; therefore, it is not possible to indicate the absorbed energy at the moment of failure in terms of a specific value. This is why the results are illustrated as a plot of absorbed energy

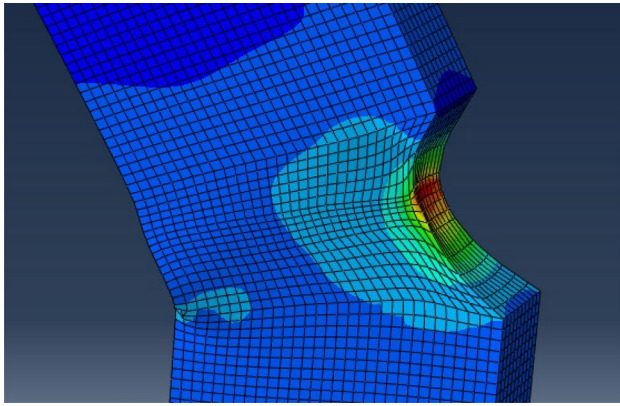


Fig. 24 Model deformation across the notched area in the course of impact test simulation

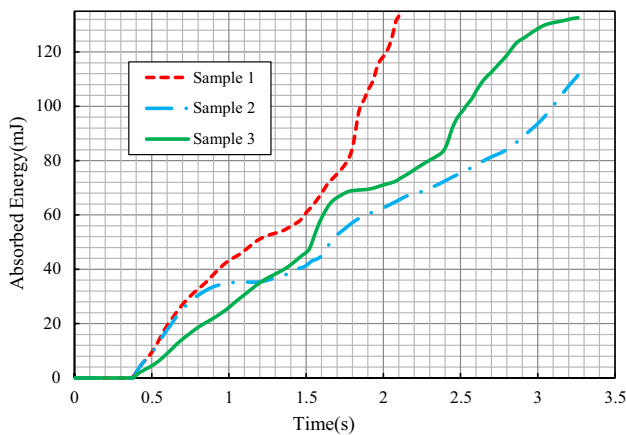


Fig. 25 Energy-time plot, specimens 1, 2, and 3

versus time. Since no fracture criteria were integrated in the constitutive models, the Izod impact simulation results present little relevance. As shown in the figures, the value of impact energy within 0–0.5 s is observed to be zero; this time interval represents the time before the pendulum collide to the specimen.

With a low percentage error, the results of simulation were found to be close to test data.

5 Conclusion

In this study, finite element simulation was utilized to obtain mechanical properties of porous polymeric nanocomposites before undertaking corresponding tests; this approach may help reducing the cost of sample preparation and save the time of performing actual tests. As mentioned, the specimens were produced by mixing molten in an extruder before being injection molded according

to the corresponding standards to tensile loading tests, three-point bending test, and Izod impact test. Once finished with performing the tests, Abaqus FEA software was utilized to simulate tensile test, three-point bending test, and Izod impact test. In the undertaken simulations, different models of a hyperelastic material were considered. After plotting the stress–strain curves which obtained from the tensile test and those of simulation of the tensile test with different models, the percentage errors of elasticity modulus, yield strength, and ultimate strength with the corresponding bar charts were drawn. Comparing the results, the best convergence to the data obtained from tensile test, three-point bending test, and Izod impact test was observed to be those with Marlow model without plasticity. The observations released that in all simulations the Marlow model had acceptable adaptation with experimental parameters. Also, adding nanoparticles (MCM-41 and PP-GMA) to polypropylene improved the mechanical properties of specimens such as yield stress and ultimate stress. Although using the second order elements, rather than linear elements, considerably increased the time to have simulation runs performed, but it was observed that for the sake of bending, torsion, and other complex loading regimes, the second order elements are the only alternatives which lead to relatively acceptable results. Due to considerable dispersion observed with linear meshing, the corresponding results would not exhibit an acceptable convergence; this is while with the second order meshing, the desired convergence was achieved. Investigation of the effect of friction coefficient on the force–displacement curve corresponding to three-point bending test revealed that the lower the friction coefficient, the smaller will be the area under force–displacement curve. The results further demonstrated that we can improve the mechanical properties of specimens, particularly in the course of three-point bending test and Izod impact test, by introducing nanoparticles, particularly a mix of mesoporous silica/hydroxyapatite, into them.

Acknowledgments We are thankful to Iran polymer and petrochemical institute for their help and assistance during the experimental process.

References

1. Arriaga A, Lazkano JM, Pagaldai R, Zaldua AM, Hernandez R, Atxurra R, Chrysostomou A (2007) Finite-element analysis of quasi-static characterisation tests in thermoplastic materials: experimental and numerical analysis results correlation with ANSYS. *Polym Test* 26:284–305
2. Tvergaard V, Needleman A (2008) An analysis of thickness effects in the Izod test. *Int J Solids Struct* 45:3951–3966
3. Viot P (2009) Hydrostatic compression on polypropylene foam. *Int J Impact Eng* 36:975–989

4. Avalle M, Belingardi G, Montanini R (2001) Characterization of polymeric structural foams under compressive impact loading by means of energy-absorption diagram. *Int J Impact Eng* 25(455):472
5. Bouix R, Viot P, Lataillade J (2009) Polypropylene foam behaviour under dynamic loadings: strain rate, density and microstructure effects. *Int J Impact Eng* 36:329–342
6. Chen W, Lu ZX, Pan B, Guo JH, Li YJ (2012) Nonlinear behavior of bumper foams under uniaxial compressive cyclic loading. *Mater Des* 35:491–497
7. Rajagopal KR, Srinivasa AR (2000) A thermodynamic framework for rate type fluid models. *J Non Newton Fluid Mech* 88:207–227
8. Danielsson M, Parks DM, Boyce MC (2004) Constitutive modeling of porous hyperelastic materials. *Mech Mater* 36:347–358
9. Demiray S, Becker W, Hohe J (2006) Analysis of two and three-dimensional hyperelastic model foams under complex loading conditions. *Mech Mater* 38:985–1000
10. Colloca M, Gupta N, Porfiri M (2013) Tensile properties of carbon nanofiber reinforced multiscale syntactic foams. *Compos B* 44:584–591
11. Othman A, Abdullah S, Ariffin AK, Mohamed NAN (2016) Investigating the crushing behavior of quasi-static oblique loading on polymeric foam filled pultruded composite square tubes. *Compos B* 95:493–514
12. Garrido M, Correia JR, Keller T (2015) Effects of elevated temperature on the shear response of PET and PUR foams used in composite sandwich panels. *Constr Build Mater* 76:150–157
13. Gover RB, Oloyede A, Thambiratnam DP, Thiyahuddin MI, Morris A (2015) Experimental and numerical study of polymeric foam efficacy in portable water filled barriers. *Int J Impact Eng* 76:83–97
14. Koohbor B, Kidane A, Lu WY, Sutton MA (2016) Investigation of the dynamic stress–strain response of compressible polymeric foam using a non-parametric analysis. *Int J Impact Eng* 91:170–182
15. Ferkl P, Pokorný R, Kosek J (2014) Multiphase approach to coupled conduction-radiation heat transfer in reconstructed polymeric foams. *Int J Therm Sci* 83:68–79
16. Bonet J, Wood RD (1997) *Nonlinear continuum mechanics for finite element analysis*. Cambridge University Press, Cambridge
17. Shabana AA (2008) *Computational continuum mechanics*. Cambridge University Press, Cambridge. doi:[10.1017/CBO9780511611469](https://doi.org/10.1017/CBO9780511611469)
18. *Abaqus Analysis User's Manual* (2009) Volume III. Dassault Systèmes Simulia Corp., Providence, RI, USA
19. British Standard BS EN ISO 527-2 (1996) *Plastics—determination of tensile properties*
20. British Standard BS 903-5 (2004) *Physical testing of rubber—Part 5: guide to the application of rubber testing to finite element analysis*
21. Marlow RS (2003) A general first-invariant hyperelastic constitutive model. In: *Constitutive models for rubber III*, Balkema Publishers, UK
22. ASTM International D 790-03 (2003) *Standard test methods for flexural properties of unreinforced and reinforced plastics and electrical insulating materials*